Breakup of elongated droplets in microfluidic T-junctions

Haringa, Cees; De Jong, Conrad; Hoang, Duong A.; Portela, Luis M.; Kleijn, Chris R.; Kreutzer, Michiel T.; Van Steijn, Volkert

Important note
To cite this publication, please use the final published version (if applicable).
Please check the document version above.

Breakup of elongated droplets in microfluidic T-junctions

Cees Haringa,[*] Conrad de Jong,[*] Duong A. Hoang, Luis M. Portela, Chris R. Kleijn,
Michiel T. Kreutzer, and Volkert van Steijn[†]

*Faculty of Applied Sciences, Delft University of Technology, van der Maasweg 9,
2629 HZ Delft, the Netherlands*

We show experimentally, and explain theoretically, what velocity is needed to break an elongated droplet entering a microfluidic T-junction. Our experiments on short droplets confirm previous experimental and theoretical work that shows that the critical velocity for breakup scales with the inverse of the length of the droplet raised to the fifth power. For long elongated droplets that have a length about thrice the channel width, we reveal a drastically different scaling. Taking into account that a long droplet remains squeezed between the channel walls when it enters a T-junction, such that the gutters in the corners of the channel are the main route for the continuous phase to flow around the droplet, we developed a model that explains that the critical velocity for breakup is inversely proportional to the droplet length. This model for the transition between breaking and nonbreaking droplets is in excellent agreement with our experiments.

I. INTRODUCTION

Bubbles and droplets of micrometer size are useful for applications in biotechnology, material synthesis, energy conversion, optofluidics, and medicine [1–5]. They can, for instance, be used to produce advanced materials such as contrast agents [6], tissue [7], (solid) foams [8], and capsules for the delivery of pharmaceuticals, nutrients, or fragrances [9–14]. Another interesting application area is the use of droplets as miniature reaction vessels for high-throughput screening [15–17] to optimize conditions or biological strains in chemical and biotechnological applications [18–23]. For almost all of these applications it is important that the behavior of bubbles or droplets in a network of microchannels is well understood [24]. This paper focuses on the behavior of droplets arriving at a branching channel, where they may break up.

In a seminal paper, Link *et al.* [25] addressed the question at what velocity a droplet of a given length breaks when flowing into a branching channel. For confined systems, the velocity is generally made dimensionless as the capillary number $Ca = \mu_c U/\gamma$, with U the arrival velocity of the droplet, μ_c the viscosity of the continuous phase, and γ the interfacial tension. Assuming breakup to occur through a Rayleigh-Plateau instability, Link *et al.* [25] showed that, while breakup in unconfined systems [26,27] is governed by the viscosity contrast λ and the capillary number Ca, breakup under confinement also depends on the level of confinement characterized by the ratio between the initial length l_0 of the droplet and the width w of the channel. The critical capillary number Ca_{cr} at the transition between breaking and nonbreaking droplets, hence, takes the form $Ca_{cr} = f(l_0/w, \lambda)$. Link *et al.* [25] validated their theoretical prediction, $Ca_{cr} = \alpha(l_0/\pi w)[(l_0/\pi w)^{-2/3} - 1]$, with experiments at moderate Ca values ($4 \times 10^{-3} \leqslant Ca \leqslant 0.3$), and found good agreement for water

---
[*]These authors contributed equally to this work.
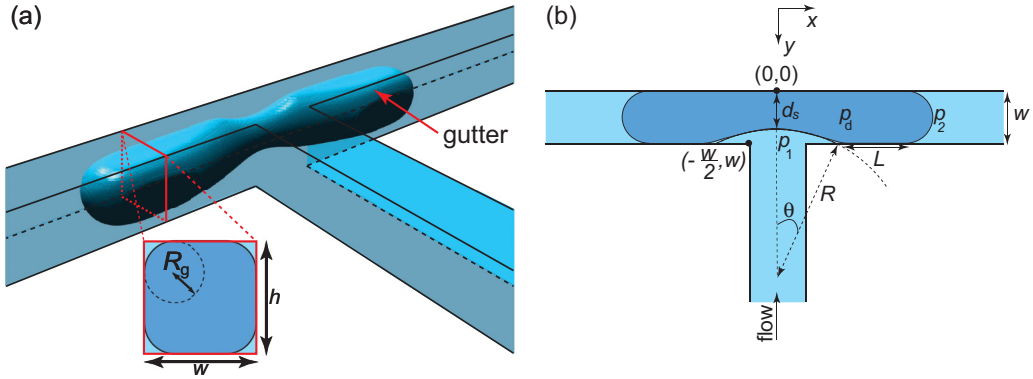[†]v.vansteijn@tudelft.nl

FIG. 1. (a) Immobile nonwetting droplet trapped inside a T-junction, the incoming continuous phase flows around the droplet through the gutters in the corners of the channels. (b) Sketch of the top view showing the shape of a concave droplet; its central part assumes a circle characterized by the neck thickness d_s, the radius R, and the (apparent) angle θ between the droplet and the channel wall.

droplets in hexadecane ($\lambda = 0.33$) when using a viscosity-dependent fit constant $\alpha = 1$. De Menech [28] confirmed this transition using three-dimensional (3D) simulations in the range $0.03 \leqslant$ Ca $\leqslant$ 0.2, and showed that α depends on the viscosity contrast. A crucial feature of the analysis based on a Rayleigh-Plateau instability is that it predicts that droplets with initial length $l_0 \geqslant \pi w$ break, even if the forces pulling on them become vanishingly small in the limit Ca $\to 0$. This prediction clearly is at odds, both with the experimental data by Jullien *et al.* [29] featuring droplets with an initial length $l_0 \approx 5w$ that do not break, and with what we know about stagnant confined droplets: the Rayleigh-Plateau instability is suppressed when a droplet touches walls on all sides.

An alternative analysis was developed by Leshansky and Pismen [30], who considered short quasistatic two-dimensional (2D) droplets, for which setting a Rayleigh-Plateau instability is not operative. To predict the critical capillary number for breakup, they analyzed for which droplet shapes the pressure drop over the droplet due to capillarity can be matched with the pressure drop due to viscous flow of the continuous phase, around the droplet, through the narrow lubricating film between the droplet and the channel wall. They found $\mathrm{Ca}_{cr} = (l_0/aw)^{-b}$, with $a = 1.3$ and $b = 5$. If one allows a to be a viscosity and channel-shape-dependent fitting parameter in applying this 2D theory to 3D experiments, this functional form of the breakup criterion agrees well with experimental data for short droplets and moderate values of Ca [29,31,32].

An important difference between the mechanisms governing the (steady) shape of short and long droplets is that short droplets do not remain in contact with all four channel walls when deformed, while long droplets do. For short droplets, the main path for the continuous phase to flow around a droplet is the resulting gap between droplet and walls, while so-called "gutters" form the main path in case of long droplets [see Fig. 1(a)]. To complement Leshansky's model developed for short droplets [30], Jullien *et al.* [29] developed a breakup criterion for long droplets. They postulated that breakup is inevitable when a droplet maintains contact with all four walls during deformation, resulting in a criterion that solely depends on λ, not on Ca. As pointed out by the authors, their purely geometrical definition of breakup overlooks the possibility that the continuous phase may flow around the droplet along the corners of the microchannel, a key notion to obtain long stable droplets trapped in a T-junction without breaking. Although Jullien's breakup criterion seems to be in reasonable agreement for their limited data range at low Ca, we show in this paper that it is essential to consider gutter flow, which is most relevant at low Ca [33–35], to capture the breakup-nonbreakup transition for long droplets.

In this paper, we start by testing the hypothesis that, at sufficient low velocities, droplets get trapped inside a T-junction while the carrier fluid continuously flows from the main channel, through

the gutters around the droplet, into the two daughter channels. Although trapping of droplets has been demonstrated in other types of geometries such as a backward-facing step [36] and so-called ladders [37,38] and anchors [39], experimental evidence of droplets trapped for the situation shown in Fig. 1 has so far not been presented. After showing experimental evidence of the existence of stable, nonbreaking droplets trapped in microfluidic T-junctions, which highlights the importance of gutter flow at low Ca, we present experiments that (1) confirm the previously found scaling $Ca_{cr} \sim (l_0/w)^{-5}$ for short droplets, which break at moderate Ca, at which gutter flow is negligible, and (2) reveal a drastically different scaling $Ca_{cr} \sim (l_0/w)^{-1}$ for long droplets, for which the transition between breaking and nonbreaking occurs at low Ca. In the last part of the paper, we explain this observed scaling for long droplets with an experimentally validated semiempirical model.

II. EXPERIMENTAL SETUP

The design of our microfluidic device is shown in Fig. 2(a). The inlet channels of water and oil are, respectively, $450\,\mu$m and $300\,\mu$m wide. They are connected by a small $100\,\mu$m wide and $100\,\mu$m long nozzle as shown in the close-up. All channels are $300\,\mu$m high, except for the $150\,\mu$m high nozzle. This semi-3D nozzle is shown in the second close-up and enables the formation of a single droplet, as explained later. The main channel of the T-junction and its side arms have equal width and height: $w = h = 300\,\mu$m. The bypass channel around the T-junction minimizes asymmetries in flow in the two side arms that arise from small differences in dimensions; see Hoang *et al.* [40] for a detailed explanation.

Fabrication of the microfluidic device is done using standard soft lithography techniques. In short, we spin coat a $150\,\mu$m thick layer of photoresist (SU-8 2100) on a silicon wafer and expose it through a transparency with the device design shown in Fig. 2(a). Before developing this layer, we spin coat a second $150\,\mu$m thick layer of photoresist on top and expose it through a second transparency. The only difference between the transparencies is that the small connection between the water and oil inlet is nontransparent on the second one. After developing the wafer, all features are $300\,\mu$m high, except for the connection between the water and oil channel, which is $150\,\mu$m high and forms the nozzle. We create a PDMS device from this wafer using a standard PDMS replication method and bond the device on a PDMS-coated glass slide. After bonding, we coat the channels by injecting a commercial Aquapel® solution in the channels and incubating them for at least 1 min, then rinsing them with FC-3823 oil, and drying them with pressurized air. After coating, oil fully wets the walls, and we do not observe direct contact between the walls and the water droplet in the form of dewetting patterns or contact lines as reported for partially wetting systems. We do note that the coating deteriorates over time, and, hence, it is important to perform the experiments within ~12 h.

The working fluids are milliQ water as the disperse phase and perfluorodecalin as the continuous phase. The perfluorodecalin solution was stabilized using 10 wt% 1H,1H,2H,2H- perfluoro-1-octanol, which reduces the interfacial tension and enhances wetting of the walls by the oil. This solution has a viscosity of $\mu_c = 7.2$ mPas such that the viscosity contrast $\lambda = \mu_d/\mu_c = 0.14$. The oil-water interfacial tension is $\gamma = 17.9$ mN/m. As we perform a measurement series with one and the same droplet, we note that it is important to presaturate the oil phase with water before use, to make the decrease in droplet volume due to dissolution negligible.

Imaging is done using a Teledyne Dalsa Falcon 2 12M (4096×3072 pixels) camera in combination with a Teledyne X64 Xcelera-CL+ PX8 Full camera link frame grabber. The camera is mounted on an internally illuminated Zeiss Axiovert S100 microscope. The images taken with this camera through a $5\times$ microscope objective have a spatial resolution of 342 pixels over the $300\,\mu$m wide channels, such that the droplet shape, characterized by the steady neck thickness d_s and the apparent contact angle θ, can be accurately measured. The angle is determined by fitting a circle through the interface, which provides the radius R and the location where the circle intersects with the channel wall [see Fig. 1(b)], from which θ is calculated.
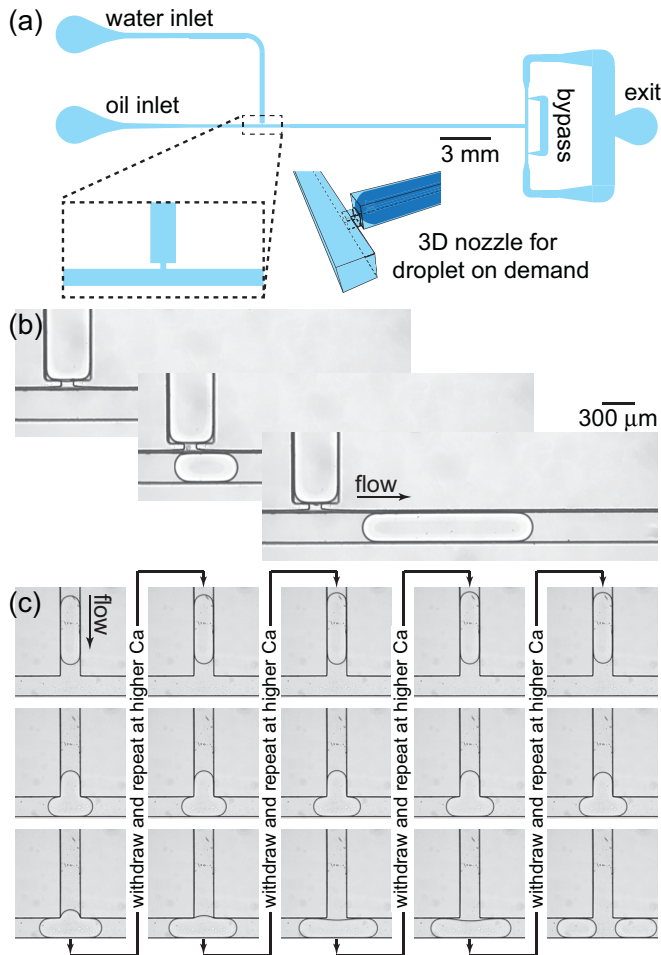
FIG. 2. (a) Device design showing two separate inlets for oil and water, the semi-3D nozzle used to form a single droplet of a given length, a T-junction in which the droplet either breaks or deforms until it reaches a steady shape, and a bypass surrounding the T-junction to minimize asymmetries in the flow in the two branches of the T-junction. (b) Three frames illustrating the formation of a single droplet on demand. (c) Typical droplet breakup experiment in which a droplet is pushed into the T-junction at relatively low velocity and reaches a steady shape (bottom left), then is repeatedly withdrawn into the feed channel and pushed into the T-junction at higher velocity, until the droplet breaks (bottom right).

Our setup differs from setups previously reported in literature [25,29,40–43] for droplet breakup studies in an important way: we produce a *single* droplet and study how it breaks or reaches a steady shape in the T-junction. We note that studying steady shapes might not be possible in systems that produce a continuous stream of droplets, as a subsequent droplet can enter the T-junction before the preceding droplet reaches its steady shape.

The formation of a single droplet on demand is done using a Fluigent MFCS-4C 25/1000 mbar pressure flow controller with which the pressures at the oil and water inlet can be precisely controlled and rapidly changed. The diameter of the tubing connecting the reservoirs to the chip was chosen such that the pressure drop over the chip itself is negligible. The oil flow rate thus is directly proportional to the pressure in the reservoir, with the hydrodynamic resistance of the tube as

the proportionality constant. This design hence makes the results described in this work independent of the fluid control system used (flow rate controlled versus pressure controlled).

The procedure to form a single water droplet is as follows: we adjust the pressure in the reservoir containing the oil to a value such that the oil stops flowing, while the pressure in the reservoir containing the water is adjusted such that the oil-water interface is pushed against the nozzle [Fig. 2(b), left]. We then increase the pressure of the water reservoir for a specified time Δt such that the water flows into the main channel [Fig. 2(b), middle], after which we successively reduce the pressure in the water reservoir and increase the pressure in the oil reservoir such that a droplet pinches off in the main channel. The interface in the water inlet channel is then again at rest and pushed against the nozzle [Fig. 2(b), right]. By varying the filling time Δt, droplets of different lengths can be produced. After their formation, their velocity is controlled by adjusting the pressure in oil reservoir to the desired value. In this way, we can precisely and independently control the length and velocity of the droplets.

A typical measurement series on droplet deformation and breakup is shown in Fig. 2(c). After the formation of a single droplet, we begin by setting the pressure in the oil reservoir to a relatively low value and shoot a movie of the droplet entering the T-junction at a low speed and reaching a steady shape (bottom left). We then lower the pressure in the oil reservoir to withdraw the droplet into the feed channel, and stop withdrawal when the droplet is back near the nozzle. Withdrawal is possible with this system when placing the fluid reservoirs lower than the outflow of the microfluidic device, such that setting the gauge pressure in the reservoirs to zero results in back flow due to the hydrostatic head. We then increase the pressure in the oil reservoir, such that the droplet enters the T-junction for a second time, now at a higher velocity. We confirm that the distance between nozzle and T-junction is sufficient for the droplet to reach a steady velocity U before reentering the T-junction. We use the velocity of the droplet as measured just before it enters the T-junction to calculate the capillary number, because the the velocity difference between the droplet and the continuous phase (q_{in}/hw) that pushes it is just a few percent [44–46] for $\lambda \leqslant 1, l_0/w \geqslant 2$, and the range of Ca studied here, and hence can be ignored. Repeating this procedure, we measure the steady shapes of a droplet of a given length at increasing values of Ca up to the value where the droplet breaks (bottom right). After establishing the critical Ca (Ca_{cr}) for the first time, we repeat the procedure, now with smaller increases in Ca to refine the critical Ca. We made use of the pressure control system that allows the withdrawal of the droplet after breakup, such that the two daughter droplets can be merged, and the same droplet can be used again.

III. SCALING OF THE CRITICAL CAPILLARY NUMBER AT LOW Ca

We start by highlighting the presence of gutter flows at low Ca. The images in the bottom row of Fig. 2(c) show experimental evidence of a stable, nonbreaking water droplet trapped in a T-junction. While this droplet seems to visually obstruct the channel on microscopy images, the continuous phase continuously flows around it through the gutters without breaking it. This observation immediately shows that the purely geometric breakup criterion postulated by Jullien *et al.* [29] needs revision. Before addressing how the flow through the gutters leads to the scaling of the transition between breaking and nonbreaking long droplets at low Ca, we first experimentally confirm the previously found scaling $\text{Ca}_{cr} \sim (l_0/w)^{-5}$ for moderate Ca, at which gutter flow is negligible.

Figure 3 shows whether a droplet of given length and speed breaks, with nonbreaking droplets in blue squares, and breaking droplets in red circles. We have done few experiments for short droplets ($l_0/w < 3$), only to reproduce what others have found: their breakup is well described by the $\text{Ca}_{cr} \sim (l_0/w)^{-5}$ scaling (solid line). For long droplets with the transition between breaking and nonbreaking occurring at low Ca, however, the transition strongly deviates from this scaling. The breakup map in Fig. 3 reveals that the scaling tends to $\text{Ca}_{cr} \sim (l_0/w)^{-1}$ for low Ca, which is in excellent agreement with the model [Eq. (9), dashed line] presented next.
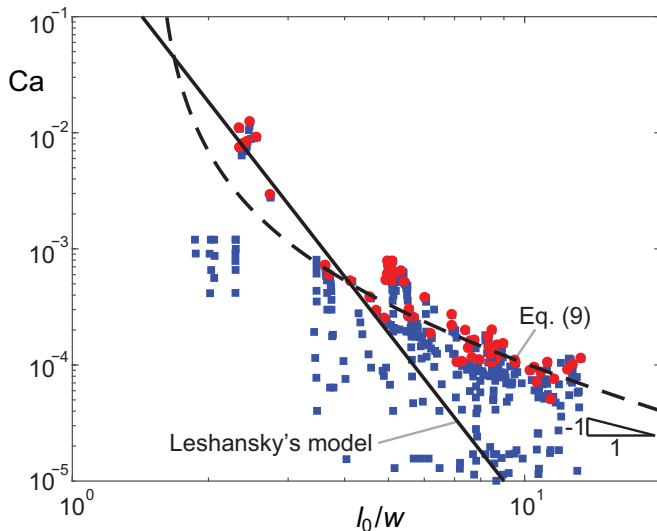
FIG. 3. Breakup map of Ca versus the dimensionless length l_0/w showing nonbreaking droplets in blue squares, and breaking droplets in red circles for a viscosity contrast $\lambda = \mu_d/\mu_c = 0.14$. For the shortest droplets ($l_0/w < 3$), the data set confirms Leshansky's theory, $l_0/w = a\mathrm{Ca}_{cr}^{-1/5}$, with fitting constant $a = 0.9$. For long droplets, the scaling of the transition line is significantly different and well captured by the model developed here [Eq. (9), with constants $c_1 = 2 \times 2.6 \times 10^{-4}$ and $c_2 = 0.25$]. The triangle shows that the scaling predicted with Eq. (9) tends to $\mathrm{Ca}_{cr} \sim (l_0/w)^{-1}$ for the lowest values of Ca. The overlap between breaking and nonbreaking data in the transition zone is attributed to fluctuations present in the experiments, for example, in the pressure that drives the continuous phase.

IV. THEORETICAL BREAKUP CRITERION FOR LONG DROPLETS

A. Momentum balance over the gutters of a trapped droplet

We consider a nonwetting droplet trapped inside a T-junction [see Fig. 1(b)] and develop a model for the quasistatic shape of long droplets using an approach similar in nature to the one developed by Leshansky and Pismen [30] for short droplets. In our quasisteady-state analysis, the continuous phase flows around the droplet through the gutters, and we ignore the much smaller flow through the flat films between these gutters. The difference in curvature at the center and the fronts of the droplet results in a pressure difference, $p_1 - p_2$. This difference due to capillarity balances the viscous pressure drop over the gutters. Considering the interface of the droplet inside the T-junction, and assuming an equilibrium shape with curvature κ, the pressure difference between the inside and outside of the droplet is given by the Laplace law according to $p_d - p_1 = \gamma\kappa$. For T-junctions with $h \leqslant w$, the interface is squeezed between the top and bottom wall such that the out-of-plane radius of curvature approximately equals $h/2$. For a concave interface [Fig. 1(b)], the in-plane radius of curvature equals $-R$. Hence, $p_d - p_1 = \gamma(2/h - 1/R)$. The two fronts of the droplet are confined by the top, bottom, and side walls such that the two radii of curvature are $h/2$ and $w/2$, hence $p_d - p_2 = \gamma(2/h + 2/w)$. We neglect viscous losses due to flow inside the droplet with respect to viscous losses due to flow through the gutters, because the area for the flow of the more viscous continuous phase through the gutters is much smaller than the area for the flow of the less viscous dispersed phase inside the droplet [47]. The pressure inside the droplet is therefore taken uniform, such that the pressure drop over the gutters becomes

$$p_1 - p_2 = \gamma\left(\frac{2}{w} + \frac{1}{R}\right). \tag{1}$$

The viscous pressure drop, $p_1 - p_2$, over the gutters can be described as [48]

$$p_1 - p_2 = \frac{C\mu}{1 - \pi/4} \frac{L}{R_g^4} \frac{q_{in}}{4} \tag{2}$$

with q_{in} the volumetric flow rate of the continuous phase, R_g and L the radius and length of a gutter [see Fig. 1(b)], and C a constant. For moderate deformations of the droplet, the droplet is separated by the top and bottom wall by thin films such that the incoming continuous phase primarily flows around the droplet through the four gutters that are in direct contact with the feed channel [49]. Based on this finding, we approximate the flow rate through a single gutter as $q_{in}/4$. For static droplets in straight rectangular channels with an aspect ratio $h/w \leqslant 1$, Wong, Morris, and Radke [50] showed that the radius R_g depends on the aspect ratio according to $(R_g/h)^{-1} = f^{-1} = 1 + h/w + [(1 - h/w)^2 + \pi h/w]^{1/2}$. In this work, we consider a square cross section, for which $f \approx 0.27$. We assume that the cross sectional area of a gutter, $(1 - \pi/4)R_g^2$, does not vary along the length of the gutter and that it is independent of the capillary number. This is in sharp contrast to the cross-sectional area of the gap that forms when deforming a short droplet [30], which does depend on the capillary number.

Balancing the pressure drops, and turning to dimensionless variables where all lengths are in units of w (also in the figures to come), the momentum balance over the gutters of a trapped droplet becomes

$$2 + 1/R = \frac{4}{c_1} L\mathrm{Ca} \tag{3}$$

with $\mathrm{Ca} = \mu q_{in}/\gamma h w$ and $c_1 = 16(1 - \pi/4)f^4 h^3/C$ as a constant that characterizes the viscous resistance in the gutters, which we determine next.

B. Friction factor for the gutters

We now relate the pressure gradient and the flux through the gutters to determine c_1 using Eq. (3). Although $1/R$ is small for most flow rates, we can omit this unknown term by considering exactly that flow rate for which a droplet of given length appears undeformed [see Fig. 4(a), bottom left] such that $1/R = 0$ (and $d_s = 1$). In that case, the gutter extends all the way from the junction to the caps. Decomposing the tip-to-tip length l_0 in (1) two curved fronts, each of length $1/2$, (2) two gutters, each of length L, and (3) the width of the feed channel, 1, we find $L = l_0/2 - 1$. Hence, Eq. (3) immediately gives

$$\mathrm{Ca}_0 = \frac{c_1}{2}(l_0/2 - 1)^{-1} \tag{4}$$

with Ca_0 the capillary number for undeformed trapped droplets.

We performed experiments in which we measured the steady neck thickness for a wide range of Ca and l_0. Examples showing how the neck thickness changes with increasing Ca for a long droplet ($l_0 = 10.0$) are shown in Fig. 4(a). Plotting the neck thickness d_s versus Ca and interpolating to $d_s = 1$ for which the droplet appears undeformed, as illustrated in Fig. 4(b), gives a precise estimate of Ca_0. Determining Ca_0 for a wide range of droplet lengths ($2.3 \leqslant l_0 \leqslant 13.1$) and plotting Ca_0 versus $(l_0/2 - 1)^{-1}$, we find the expected linear relation as shown in Fig. 4(c), from which we obtained the proportionality constant $c_1/2 = 2.6 \times 10^{-4}$. We compare this experimental value with the theoretical estimate $c_1/2 = (8 - 2\pi)f^4 h^3/C = 9.1 \times 10^{-5}$, using $f = 0.27$, $h = 1$ for square channels, and $C = 93.93$ as calculated by Ransohoff and Radke [48]. This latter value was derived for a no-shear boundary condition at the interface and hence may be higher in our liquid-liquid experiments, but it certainly does not exceed a value of 248.48 derived for a no-slip boundary condition. The here observed lower resistance is consistent with earlier observations [51]. The theoretical value holds for gutters around static droplets, whereas under flowing conditions (1) a
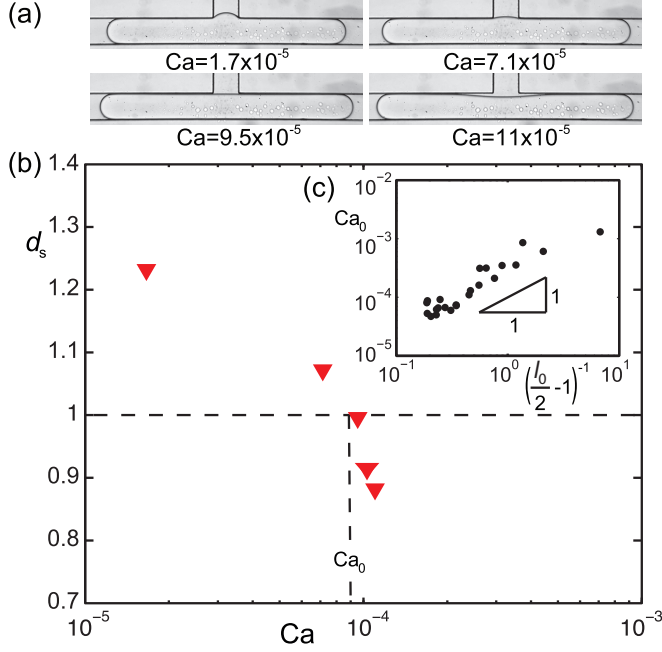
FIG. 4. (a) Steady droplet shapes for a long droplet ($l_0 = 10.0$) at increasing values of the capillary number. (b) Steady neck thickness as a function of Ca. The capillary number Ca_0 corresponding to an undeformed droplet was determined as illustrated. (c) Log-log plot showing the expected linear dependence of Ca_0 on $(l_0/2 - 1)^{-1}$.

lubricating film connects the gutters and (2) the fluid in those films drains towards the gutters, that grow as a result [52]. Both phenomena increase the gutter size and lower the resistance to flow.

C. Equilibrium shape of concave droplets

For a concavely deformed droplet, we describe the 2D projection of the central part of the droplet interface in the T-junction with a circular arc. This shape is fully characterized by two parameters, for example, the radius R and the angle θ [Fig. 1(b)]. To predict the shape of the droplet using the momentum balance [Eq. (3)], we, hence, need to establish additional relations between d_s, L, θ, and R.

The circular description of the central part of the droplet directly relates R, θ, and d_s through

$$R = (1 - d_s)/(1 - \cos\theta). \tag{5}$$

An expression for the gutter length, L, follows from equating the volume of a droplet trapped inside the T-junction to the volume of the droplet before it enters the T-junction. We approximate the 2D projection of the droplet before it enters the T-junction with two half circles with dimensionless radius $1/2$, connected by a rectangular body of dimensionless length $l_0 - 1$, and then calculate the dimensionless volume V by extruding the dimensionless area $\pi/4 + (l_0 - 1)$ over the dimensionless height of the channel. Hence, $V = (\pi/4 + l_0 - 1)h$. This simplified description of the volume is most accurate for long droplets (accurate within 10% for $L \geqslant 8$) and accurate within 15% for the shortest droplets ($L = 3$) considered in this work [53]. Using a similar approach, we find $V \approx [\pi/4 + 2L + 2R\sin\theta - R^2(\theta - \sin\theta\cos\theta)]h$ for a concave droplet inside the T-junction. Equating these two volumes results in an expression for the gutter
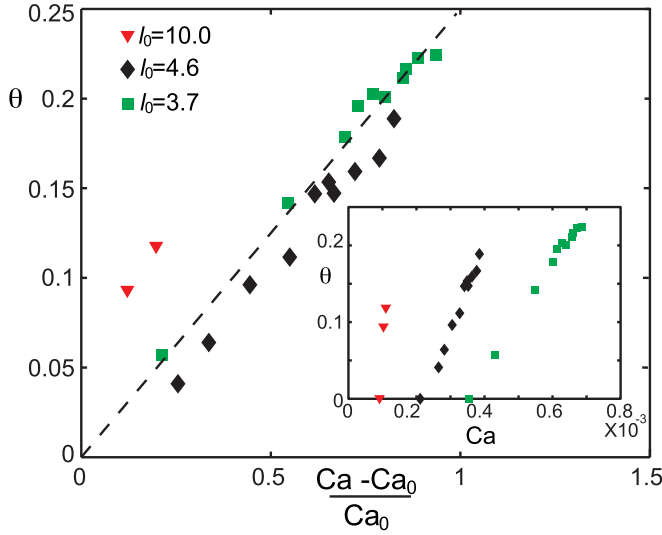
FIG. 5. Inset: Apparent contact angle of equilibrium droplets as a function of the capillary number for different droplet lengths. Main figure: All lines collapse in a plot of θ versus $(Ca - Ca_0)/Ca_0$.

length:

$$2L = (l_0 - 1) - 2R \sin \theta + R^2 (\theta - \sin \theta \cos \theta). \tag{6}$$

The remaining question that needs to be addressed, before we can predict the equilibrium shape of a droplet entering the T-junction at a given speed and length, is how the angle θ depends on these parameters. We obtained this relation experimentally by measuring the apparent contact angles and plotting them against Ca for droplets of different lengths in the inset of Fig. 5. The data show that $\theta = 0$ for a finite value $Ca = Ca_0$. Furthermore, the dependence of θ on Ca appears to be linear. It should be noted, though, that the maximum observed angle is below 0.25, such that nonlinear effects, when present, are hard to detect. Knowing that the angle equals zero for $Ca = Ca_0$, the angle likely depends on the difference $Ca - Ca_0$. We indeed find that the data for different droplet lengths collapse on a straight line when plotting θ versus the normalized difference $(Ca - Ca_0)/Ca_0$ as shown in the main graph of Fig. 5, although with a slight deviation for $l_0 = 10$. Based on this experimental data set, we use the empirical relation

$$\theta = c_2 \frac{Ca - Ca_0}{Ca_0} \tag{7}$$

with fitting constant $c_2 \approx 0.25$. The universality of this constant, together with the theoretical foundation of this empirical relation, remains to be established in future work.

How the steady shape of a droplet depends on its speeds and initial length is now fully captured by Eqs. (3)–(7). Solving this set (numerically) for d_s, we find good agreement between experimental data (symbols) and this model (solid lines) as shown in Fig. 6, where we used the values of c_1 and c_2 as established before.

In the last part of the paper, we provide the theoretical foundation for the scaling of the experimentally observed transition line $Ca_{cr} \propto l_0^{-1}$. To this end, it is helpful to first introduce three simplifications that enable us to analytically derive this relation from the full model [Eqs. (3)–(7)] and to show the validity of these simplifications. The first simplification is to neglect the $1/R$ term in Eq. (3), justified by the observation that in all our experiments with long droplets, we have seen that $1/R \ll 2$. This is not surprising: critical capillary numbers are much smaller for long droplets than for short droplets, such that surface tension can better resist a change in curvature in the center.
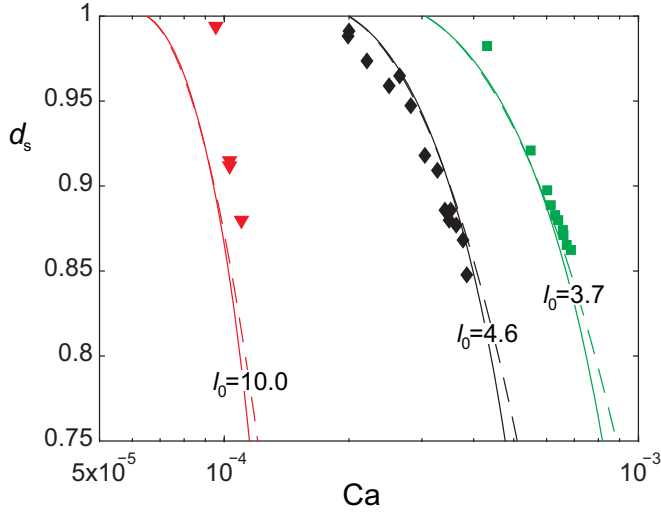
FIG. 6. The steady neck thickness of concave droplets of three different initial lengths as a function of the capillary number. The experimental data (symbols) agree well with the full theoretical model [solid lines, Eqs. (3)–(7)] and with the simplified model [dashed lines, Eq. (8)], $c_1 = 2 \times 2.6 \times 10^{-4}$, $c_2 = 0.25$.

Two additional simplifications are based on the observation that angles are generally small ($\theta \ll 1$) such that (1) the term containing $\theta - \sin\theta \cos\theta = \theta^3 + O(\theta^5)$ in Eq. (6) can be neglected and (2) the term $(1 - \cos\theta)/2\sin\theta$ [obtained after elimination of R by substitution of Eq. (5) in Eq. (6) and rearranging the resulting equation to express d_s in terms of the other variables] can be expanded to $\theta/4 + O(\theta^3)$. Using these simplifications, and dropping the $O(\theta^2)$ and higher order terms, the full model reduces to

$$d_s = 1 - \frac{c_2}{4c_1} \text{Ca}(l_0 - 2 - c_1 \text{Ca}^{-1})(l_0 - 1 - c_1 \text{Ca}^{-1}). \tag{8}$$

This simplified model description is also plotted in Fig. 6 as the dashed lines and shows good agreement with the full model, supporting the validity of the simplifications and Eq. (8).

D. Breakup transition

Being able to predict the equilibrium shape of concave droplets trapped in a T-junction for a given combination of Ca and l_0 using the full [Eqs. (3)–(7)] and simplified model [Eq. (8)], we are close to predicting the transition between breaking and nonbreaking droplets. The remaining question is what the maximum deformation is before a droplet breaks. As it turns out, there exists a critical neck thickness, d_{sc}, below which it is not possible to obtain a steady droplet shape. In contrast to the finding that $d_{sc} = 0.5$ for short 2D droplets [30], our experiments in a 3D T-junction with $h = 1$ show that the critical neck thickness is significantly larger. Based on the last data point in each data set in Fig. 6, we see that the critical neck thickness is roughly independent of the initial droplet length and equal to $d_{sc} \approx 0.85$. How much the neck of a droplet can be deformed in the junction before it autonomously breaks is known to depend on the level of confinement [49], and we hence expect the value of d_{sc} to be different for junctions with other aspect ratios.

The transition between breaking and nonbreaking droplets can now be predicted. For a droplet of a given length, l_0, the neck thickness reaches the critical neck thickness at the critical capillary number. Substituting $d_s = d_{sc}$ and Ca = Ca_{cr} in Eq. (8) and rewriting it in the form $l_0 = f(Ca_{cr})$,

(a)

Ca= 7.5×10^{-5} 1.7×10^{-4} 3.5×10^{-4} 6.0×10^{-4} 6.9×10^{-4}

(b)

Ca= 3.2×10^{-5} 2.3×10^{-4} 6.1×10^{-4} 1.6×10^{-3} 2.7×10^{-3}
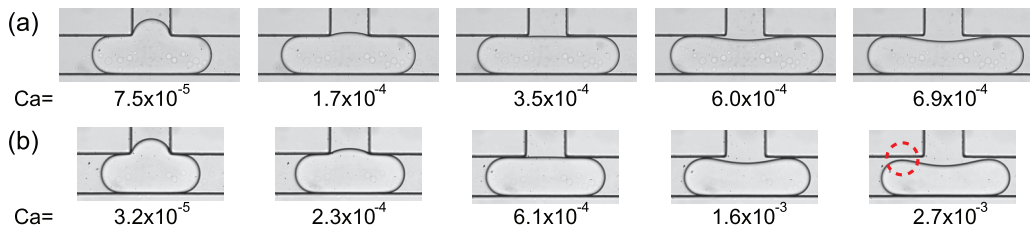
FIG. 7. Steady neck thickness as a function of Ca, for two relatively short droplets. (a) A droplet with length $l_0 = 3.6$ fully spans the channel width up to the critical capillary number at which it breaks, with its shape consistent with the one assumed in our model. (b) A shorter droplet with initial length $l_0 = 2.8$ is no longer fully squeezed between the walls; before reaching the critical capillary number for breakup, a "tunnel" opens as shown in the right most picture; note that this picture is the only nonequilibrium shape, and the droplet moved into in the right branch immediately after taking the image.

we find the transition line

$$l_0 = \frac{3}{2} + c_1 \mathrm{Ca}_{cr}^{-1} + \frac{1}{2} \left[1 + \frac{16}{c_2} c_1 \mathrm{Ca}_{cr}^{-1} (1 - d_{sc}) \right]^{1/2}$$

$$\approx \frac{3}{2} + c_1 \mathrm{Ca}_{cr}^{-1} + \left[\frac{4c_1}{c_2} (1 - d_{sc}) \right]^{1/2} \mathrm{Ca}_{cr}^{-1/2}. \tag{9}$$

This relation shows that for $\mathrm{Ca} \ll c_1 c_2 / 4 (1 - d_{sc}) \approx 10^{-4}$ the droplet length at the transition between breaking and nonbreaking droplets scales as $l_0 \propto \mathrm{Ca}_{cr}^{-1}$, insensitive to the exact values of d_{sc} and c_2. As shown in Fig. 3, this transition line (dashed) agrees well with the experimental data for long droplets and low Ca and shows that the slope of the predicted transition line is already close to -1 in the log-log plot for $\mathrm{Ca} = 10^{-4}$ and further approaches a slope of -1 for lower Ca. Good agreement is observed for droplets longer than about $l_0 > 3$. This is in line with the observation that such droplets take the shape assumed in our model up to the critical capillary number, as shown in Fig. 7(a). Shorter droplets close to the critical point have a shape that deviates from the model shape, as their volume simply does not permit them to fully span the channel width during their compression; see Fig. 7(b). Our model, hence, complements Leshansky's model [30], for droplets longer than roughly thrice the channel width.

We conclude this section by noting that this paper is entirely about the breakup-nonbreakup transition. At this transition, long droplets, both breaking and nonbreaking, appear to visually obstruct the channel on microscopy images and can thus be classified as "nonbreaking with obstruction" and "breaking with obstruction." Away from the transition, breaking droplets can be further classified as "breaking with obstruction" and "breaking without obstruction." The boundary between these different types of breakup is beyond the scope of the present work and is described by Jullien *et al.* [29] and Leshansky *et al.* [54] for moderate Ca.

V. CONCLUSIONS

For short droplets that break at moderate values of the capillary number, our experiments show that the transition between breaking and nonbreaking droplets is well captured by Leshansky's scaling relation developed for short droplets [30]. Expressed in the two most important dimensionless parameters, the nondimensional length l_0 and speed Ca, this scaling relation reads $l_0 \propto \mathrm{Ca}_{cr}^{-5}$. For long droplets where the transition takes place at much lower values of Ca, our experiments reveal a drastically different scaling: $l_0 \propto \mathrm{Ca}_{cr}^{-1}$. This observed scaling is in excellent agreement with our theoretical model, which takes into account that long droplets remain squeezed between the channel walls when they enter a T-junction, such that the gutters in the corners of the channel are the main route for the continuous phase to flow around the droplet. Experimental observations show that

this assumption is satisfied for droplets longer than roughly thrice the width of the channel, which explains why our model describes the experimentally found transition line well for $l_0 > 3$.

The insights of this work may be useful in other fields of research as well, for instance, in the design of multiphase flow distributors for aliquoting samples in analytical applications [55] and for parallelizing microreactors [40,56]. While these distributors are typically based on simple structures such as the T-junction as considered in this work, the insights into the critical velocity to break droplets into smaller pieces may also be useful in applications featuring more complicated geometries, such as the pore structures in which so-called ganglia may get trapped during enhanced oil recovery.

[1] A. B. Theberge, F. Courtois, Y. Schaerli, M. Fischlechner, C. Abell, F. Hollfelder, and W. T. S. Huck, Microdroplets in microfluidics: An evolving platform for discoveries in chemistry and biology, Ang. Chem. Int. Ed. **49**, 5846 (2010).

[2] A. Huebner, S. Sharma, M. Srisa-Art, F. Hollfelder, J. B. Edel, and A. J. Demello, Microdroplets: A sea of applications? Lab Chip **8**, 1244 (2008).

[3] R. Seemann, M. Brinkmann, T. Pfohl, and S. Herminghaus, Droplet based microfluidics, Rep. Prog. Phys. **75**, 016601 (2012).

[4] S.-Y. Teh, R. Lin, L.-H. Hung, and A. P. Lee, Droplet microfluidics, Lab Chip **8**, 198 (2008).

[5] Y. Xie, D. Bos, L. J. de Vreede, H. L. de Boer, M.-J. van der Meulen, M. Versluis, A. J. Sprenkels, A. van den Berg, and J. C. T. Eijkel, High-efficiency ballistic electrostatic generator using microdroplets, Nat. Commun. **5**, 3575 (2014).

[6] K. Hettiarachchi, E. Talu, M. L. Longo, P. A. Dayton, and A. P. Lee, On-chip generation of microbubbles as a practical technology for manufacturing contrast agents for ultrasonic imaging, Lab Chip **7**, 463 (2007).

[7] R. Perez and H.-W. Kim, Core-shell designed scaffolds for drug delivery and tissue engineering, Acta Biomater. **21**, 2 (2015).

[8] A. Quell, J. Elsing, W. Drenckhan, and C. Stubenrauch, Monodisperse polystyrene foams via microfluidics—A novel templating route, Adv. Eng. Mater. **17**, 604 (2015).

[9] T. Nisisako, T. Torii, T. Takahashi, and Y. Takizawa, Synthesis of monodisperse bicolored Janus particles with electrical anisotropy using a microfluidic co-flow system, Adv. Mater. **18**, 1152 (2006).

[10] D. Dendukuri and P. S. Doyle, The synthesis and assembly of polymeric microparticles using microfluidics, Adv. Mater. **21**, 4071 (2009).

[11] S. Marre and K. F. Jensen, Synthesis of micro- and nanostructures in microfluidic systems, Chem. Soc. Rev. **39**, 1183 (2010).

[12] H. C. Shum, A. R. Abate, D. Lee, A. R. Studart, B. Wang, C.-H. Chen, J. Thiele, R. K. Shah, A. Krummel, and D. A. Weitz, Droplet microfluidics for fabrication of non-spherical particles, Macromol. Rapid Comm. **31**, 108 (2010).

[13] Y. Song, Y. K. Chan, Q. M. Ma, Z. Liu, and H. C. Shum, All-aqueous electrosprayed emulsion for templated fabrication of cytocompatible microcapsules, ACS Appl. Mater. Interf. **7**, 13925 (2015).

[14] J. Zhang, R. J. Coulston, S. T. Jones, J. Geng, O. A. Scherman, and C. Abell, One-step fabrication of supramolecular microcapsules from microfluidic droplets, Science **335**, 690 (2012).

[15] A. Günther and K. F. Jensen, Multiphase microfluidics: From flow characteristics to chemical and material synthesis, Lab Chip **6**, 1487 (2006).

[16] M. T. Guo, A. Rotem, J. A. Heyman, and D. A. Weitz, Droplet microfluidics for high-throughput biological assays, Lab Chip. **12**, 2146 (2012).

[17] H. Song, D. Chen, and R. F. Ismagilov, Reactions in droplets in microfluidic channels, Ang. Chem. Int. Ed. **45**, 7336 (2006).

[18] K. Martin, T. Henkel, V. Baier, A. Grodrian, T. Schön, M. Roth, J. M. Köhler, and J. Metze, Generation of larger numbers of separated microbial populations by cultivation in segmented-flow microdevices, Lab Chip **3**, 202 (2003).

[19] B. Zheng, C. J. Gerdts, and R. F. Ismagilov, Using nanoliter plugs in microfluidics to facilitate and understand protein crystallization, Curr. Opin. Struct. Biol. **15**, 548 (2005).

[20] E. Brouzes, M. Medkova, N. Savenelli, D. Marran, M. Twardowski, J. B. Hutchison, J. M. Rothberg, D. R. Link, N. Perrimon, and M. L. Samuels, Droplet microfluidic technology for single-cell high-throughput screening, Proc. Natl. Acad. Sci. USA **106**, 14195 (2009).

[21] J. J. Agresti, E. Antipov, A. R. Abate, K. Ahn, A. C. Rowat, J.-C. Baret, M. Marquez, A. M. Klibanov, A. D. Griffiths, and D. A. Weitz, Ultrahigh-throughput screening in drop-based microfluidics for directed evolution, Proc. Natl. Acad. Sci. USA **107**, 4004 (2010).

[22] K. Leung, H. Zahn, T. Leaver, K. M. Konwar, N. W. Hanson, A. P. Pagé, C.-C. Lo, P. S. Chain, S. J. Hallam, and C. L. Hansen, A programmable droplet-based microfluidic device applied to multiparameter analysis of single microbes and microbial communities, Proc. Natl. Acad. Sci. USA **109**, 7665 (2012).

[23] S. Jakiela, T. S. Kaminski, O. Cybulski, D. B. Weibel, and P. Garstecki, Bacterial growth and adaptation in microdroplet chemostats, Ang. Chem. Int. Ed. **52**, 8908 (2013).

[24] S. L. Anna, Droplets and bubbles in microfluidic devices, Annu. Rev. Fluid Mech. **48**, 285 (2016).

[25] D. R. Link, S. L. Anna, D. A. Weitz, and H. A. Stone, Geometrically Mediated Breakup of Drops in Microfluidic Devices, Phys. Rev. Lett. **92**, 054503 (2004).

[26] G. I. Taylor, The formation of emulsions in definable fields of flow, Proc. R. Soc. Lond. A **146**, 0501 (1934).

[27] H. A. Stone, B. J. Bentley, and L. G. Leal, An experimental study of transient effects in the breakup of viscous drops, J. Fluid Mech. **173**, 131 (1986).

[28] M. DeMenech, Modeling of droplet breakup in a microfluidic T-shaped junction with a phase-field model, Phys. Rev. E **73**, 031505 (2006).

[29] M. C. Jullien, M. J. T. M. Ching, C. Cohen, L. Menetrier, and P. Tabeling, Droplet breakup in microfluidic T-junctions at small capillary numbers, Phys. Fluids **21**, 072001 (2009).

[30] A. M. Leshansky and L. M. Pismen, Breakup of drops in a microfluidic T junction, Phys. Fluids **21**, 023303 (2009).

[31] S. Afkhami, A. M. Leshansky, and Y. Renardy, Numerical investigation of elongated drops in a microfluidic T-junction, Phys. Fluids **23**, 022002 (2011).

[32] A. Bedram and A. Moosavi, Droplet breakup in an asymmetric microfluidic T junction, Eur. Phys. J. E **34**, 78 (2011).

[33] H. Wong, C. J. Radke, and S. Morris, The motion of long bubbles in polygonal capillaries. Part 2. Drag, fluid pressure and fluid flow, J. Fluid. Mech. **292**, 95 (1995).

[34] V. S. Ajaev and G. M. Homsy, Modeling shapes and dynamics of confined bubbles, Annu. Rev. Fluid Mech. **38**, 277 (2006).

[35] M. J. Fuerstman, A. Lai, M. E. Thurlow, S. S. Shevkoplyas, H. A. Stone, and G. M. Whitesides, The pressure drop along rectangular microchannels containing bubbles, Lab Chip **7**, 1479 (2007).

[36] G. Dawson, S. Lee, and A. Juel, The trapping and release of bubbles from a linear pore, J. Fluid. Mech. **722**, 437 (2013).

[37] X. Niu, S. Gulati, J. B. Edel, and A. J. deMello, Pillar-induced droplet merging in microfluidic circuits, Lab Chip **8**, 1837 (2008).

[38] P. M. Korczyk, L. Derzsi, S. Jakiela, and P. Garstecki, Microfluidic traps for hard-wired operations on droplets, Lab Chip **13**, 4096 (2013).

[39] R. Dangla, S. Lee, and C. N. Baroud, Trapping Microfluidic Drops in Wells of Surface Energy, Phys. Rev. Lett. **107**, 124501 (2011).

[40] D. A. Hoang, C. Haringa, L. M. Portela, M. T. Kreutzer, C. R. Kleijn, and V. van Steijn, Design and characterization of bubble-splitting distributor for scaled-out multiphase microreactors, Chem. Eng. J. **236**, 545 (2014).

[41] L. Ménétrier-Deremble and P. Tabeling, Droplet breakup in microfluidic junctions of arbitrary angles, Phys. Rev. E **74**, 035303 (2006).

[42] T. Fu and Y. Ma, Bubble formation and breakup dynamics in microfluidic devices: A review, Chem. Eng. Sci. **135**, 343 (2015).

[43] Y. Lu, T. Fu, C. Zhu, Y. Ma, and H. Z. Li, Dynamics of bubble breakup at a T junction, Phys. Rev. E **93**, 022802 (2016).

[44] S. Jakiela, S. Makulska, P. M. Korczyk, and P. Garstecki, Speed of flow of individual droplets in microfluidic channels as a function of the capillary number, volume of droplets and contrast of viscosities, Lab Chip **11**, 3603 (2011).

[45] S. Jakiela, P. M. Korczyk, S. Makulska, O. Cybulski, and P. Garstecki, Discontinuous Transition in a Laminar Fluid Flow: A Change of Flow Topology Inside a Droplet Moving in a Micron-Size Channel, Phys. Rev. Lett. **108**, 134501 (2012).

[46] S. S. Rao and H. Wong, The motion of long drops in rectangular microchannels at low capillary numbers, J. Fluid Mech. **852**, 60 (2018).

[47] V. van Steijn, P. M. Korczyk, L. Derzsi, A. R. Abate, D. A. Weitz, and P. Garstecki, Block-and-break generation of microdroplets with fixed volume, Biomicrofluidics **7**, 024108 (2013).

[48] T. C. Ransohoff and C. J. Radke, Laminar flow of a wetting liquid along the corners of a predominantly gas-occupied noncircular pore, J. Colloid Interf. Sci. **121**, 392 (1988).

[49] D. A. Hoang, L. M. Portela, C. R. Kleijn, M. T. Kreutzer, and V. van Steijn, Dynamics of droplet breakup in a t-junction, J. Fluid Mech. **717**, R4 (2013).

[50] H. Wong, S. Morris, and C. J. Radke, Three-dimensional menisci in polygonal capillaries, J. Colloid Interf. Sci. **148**, 317 (1992).

[51] V. van Steijn, C. R. Kleijn, and M. T. Kreutzer, Flows Around Confined Bubbles and Their Importance in Triggering Pinch-Off, Phys. Rev. Lett. **103**, 214501 (2009).

[52] A. De Lozar, A. Juel, and A. L. Hazel, The steady propagation of an air finger into a rectangular tube, J. Fluid. Mech. **614**, 173 (2008).

[53] M. Musterd, V. van Steijn, C. R. Kleijn, and M. T. Kreutzer, Calculating the volume of elongated bubbles and droplets in microchannels from a top view image, RSC Adv. **5**, 16042 (2015).

[54] A. M. Leshansky, S. Afkhami, M.-C. Jullien, and P. Tabeling, Obstructed Breakup of Slender Drops in a Microfluidic T Junction, Phys. Rev. Lett. **108**, 264502 (2012).

[55] D. N. Adamson, D. Mustafi, J. X. J. Zhang, B. Zheng, and R. F. Ismagilov, Production of arrays of chemically distinct nanolitre plugs via repeated splitting in microfluidic devices, Lab Chip **6**, 1178 (2006).

[56] N. de Mas, A. Günther, T. Kraus, M. A. Schmidt, and K. F. Jensen, Scaled-out multilayer gas-liquid microreactor with integrated velocimetry sensors, Ind. Eng. Chem. Res. **44**, 8997 (2005).